PCCP

ROYAL SOCIETY OF CHEMISTRY

PAPER

View Article Online
View Journal | View Issue

Cite this: *Phys. Chem. Chem. Phys.*, 2020, **22**, 26167

Towards accurate prediction for laser-coolable molecules: relativistic coupled-cluster calculations for yttrium monoxide and prospects for improving its laser cooling efficiencies†

Chaoqun Zhang,[a] Hannah Korslund,[a] Yewei Wu,[bc] Shiqian Ding*[bc] and Lan Cheng *[a]

Received 1st September 2020,
Accepted 20th October 2020

DOI: 10.1039/d0cp04608f

rsc.li/pccp

Benchmark relativistic coupled-cluster calculations for yttrium monoxide (YO) with accurate treatment of relativistic and electron correlation effects are reported. The spin–orbit mixing of $^2\Pi$ and $^2\Delta$ is found to be an order of magnitude smaller than previously reported in the literature. Together with the measurement of the lifetime of the $A'^2\Delta_{3/2}$ state, it implies an enhanced capability of a narrow-line cooling scheme to bring YO to sub-recoil temperature. The computed electronic transition properties also support a four-photon scheme to close the leakage of the $A^2\Pi_{1/2} \leftrightarrow X^2\Sigma_{1/2}^+$ cycle through the $A'^2\Delta_{3/2}$ state by repumping the $A'^2\Delta_{3/2}$ state to the $B^2\Sigma_{1/2}^+$ state, which subsequently decays back to $X^2\Sigma_{1/2}^+$. Relativistic coupled-cluster methods, capable of providing accurate spectroscopic parameters that characterize the local potential curves and hence of providing accurate Franck–Condon factors, appear to be promising candidates for accurate calculation of properties for laser-coolable molecules.

I. Introduction

Cold molecules have the potential to provide new avenues for quantum information science, cold chemistry, and precision tests of fundamental physics.[1–17] Laser cooling techniques offer a promising route to bring molecules towards the ultracold regime.[18–27] However, the complex internal structure of a molecule poses challenges for applying laser-cooling techniques well established for atoms. A molecule in the vibrational ground state of an electronic upper state can make transitions to a number of vibrational states of a lower electronic state, which requires the use of additional repumping lasers to form a nearly closed optical cycle. This leads to complicated molecule-specific experimental setup. The selection of a suitable molecule thus is of importance to the success of an experimental effort. While determination of molecular parameters pertinent to laser cooling mainly relies on experimental measurement using high-resolution laser spectroscopy,[28–32] calculations of these parameters aiming at identifying laser-coolable molecules have also attracted considerable attention.[33–45]

Of particular interest to laser cooling are small molecules comprising an alkaline or early/late transition metal and an electron-withdrawing ligand and possessing one unpaired electron. The $X^2\Sigma$ ground state of these molecules usually have the unpaired electron in the metal s-type orbital. The first manifold of electronically excited states consist of the $A^2\Pi$ and $A'^2\Delta$ states as well as the $B^2\Sigma$ state. Since the unpaired electrons in these excited states are also localized at the metal site, these excited states largely preserve the nature of the metal–ligand bond and exhibit geometries and vibrational structures similar to those of the ground state. This leads to diagonally dominant Franck–Condon factors (FCFs) for transitions between these excited states and the ground state, which is crucial for forming closed optical cycles. Many polar molecules studied in the field of laser cooling fall into this category.[18–25]

Perhaps the most important molecular properties in the context of laser cooling for these molecules are the FCFs for the dipole-allowed $A^2\Pi \leftrightarrow X^2\Sigma$ and $B^2\Sigma \leftrightarrow X^2\Sigma$ transitions as candidates to form closed optical cycles. Pertinent to accurate calculations of FCFs are the local potential energy curves (PECs) around the equilibrium geometries. Therefore, the most important criterion for selecting methods for calculating electronic structures is the capability of providing accurate spectroscopic parameters that characterize the local PECs, *i.e.*, equilibrium

[a] *Department of Chemistry, The Johns Hopkins University, Baltimore, MD 21218, USA. E-mail: lcheng24@jhu.edu*
[b] *JILA, National Institute of Standards and Technology and the University of Colorado, Boulder, Colorado 80309-0440, USA. E-mail: shiqian.ding@colorado.edu*
[c] *Department of Physics, University of Colorado, Boulder, Colorado 80309-0390, USA*

† Electronic supplementary information (ESI) available. See DOI: 10.1039/d0cp04608f

structures, harmonic vibrational frequencies, as well as cubic and quartic force constants. Further, the level positions of the $A'^2\Delta$ states and the transition intensities between $A^2\Pi$ and $A'^2\Delta$ are also of significant interest. They are responsible for whether the $A^2\Pi \leftrightarrow X^2\Sigma$ cycle has a significant leakage to the "dark" $A'^2\Delta$ state. Finally, accurate calculation of spin–orbit mixing between $A'^2\Delta$ and $A^2\Pi$ plays an important role in determining the lifetime and transition properties of the $A'^2\Delta$ states, which is relevant to narrow-line cooling techniques using the $A'^2\Delta$ state[46] or repumping schemes to reduce the effects due to leakage of the $A^2\Pi_{1/2} \leftrightarrow X^2\Sigma_{1/2}$ cycle to the $A'^2\Delta_{3/2}$ state.

The present work reports a benchmark computational study of the above-mentioned properties pertinent to laser cooling of yttrium monoxide (YO)[20,47–49] together with prospects for enhancing laser cooling efficiencies for this molecule. Since the prospect schemes use the $A'^2\Delta$ state, the treatment of spin–orbit effects on the lifetime and transition properties of the $A'^2\Delta$ state is one focus of the present computational study. An experimental measurement of the $A'^2\Delta$ lifetime is also reported. The implication of $A'^2\Delta$–$A^2\Pi$ spin–orbit mixing to a narrow-line cooling scheme of YO proposed in ref. 46 and a new idea of using the $B^2\Sigma_{1/2}^+ \leftrightarrow A'^2\Delta_{3/2}$ transition to close the leakage to the $A'^2\Delta_{3/2}$ from the $A^2\Pi_{1/2} \leftrightarrow X^2\Sigma_{1/2}^+$ cycle are discussed. Another focus of the present study is to use the hierarchies of coupled-cluster methods and systematically expanded basis sets to evaluate the convergence of computational results. A variety of forms for potential energy curves, including *ab initio* potential, harmonic potential, and Morse potential, have also been used in calculations of Franck–Condon factors to study the effects of the potential function. These analyses as well as comparison with experimental measurements of YO[50–57] aim to assess the accuracy of computed properties, paving the way to quantitative calculations with predictive value.

II. Methods

A. Experimental

The experimental method reported here focuses on lifetime measurement of the $A'^2\Delta_{3/2}$ state *via* observing fluorescence of YO following exciting the molecules to $A'^2\Delta_{3/2}$. A YO molecular beam at a speed of 100 m s^{-1} is generated with a buffer gas cell[58] filled with helium at 4 K temperature. The excitation is achieved with a resonant laser pulse at 689.6 nm, which is produced with a laser diode and inherits a 2 kHz linewidth through offset-phase-locking[59] to a narrow-line laser used for cooling Sr atoms.[60] The laser pulse, with a duration of 60 μs and intensity of 3.5 mW cm^{-2}, is applied perpendicular to the molecular beam and resonantly drives the transition $X^2\Sigma_{1/2}^+$, $v = 0$, $N = 0$, $G = 0$, $F = 0$ to $A'^2\Delta_{3/2}$, $v' = 0$, $J' = 3/2(-)$, $F' = 1$.[46] After switching off the laser light, we collect the fluorescence of the molecules with a photomultiplier tube. We assume the fluorescence (shown in Fig. 1) to decay exponentially, and extract the lifetime to be 23(2) μs.

B. Computational

The CFOUR program package[61–67] has been used in all computations presented here (Fig. 2). The electron configurations of

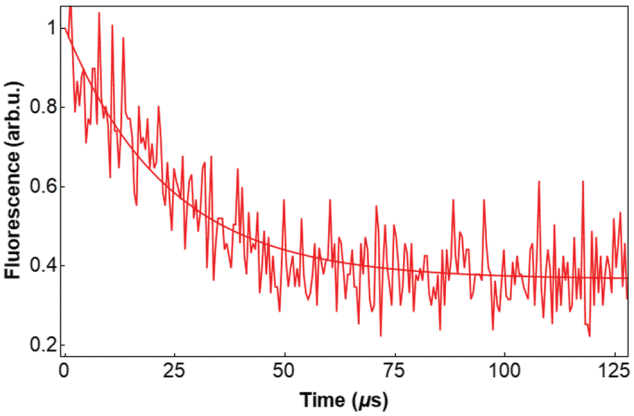

Fig. 1 Measurement of $A'^2\Delta_{3/2}$ lifetime τ. The jagged line represents the experimental data and the smooth line is a fit to the function $ae^{-t/\tau} + b$, where a and b are constants.

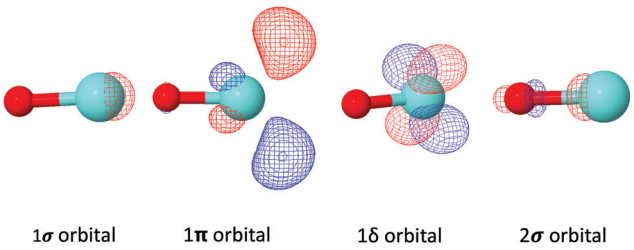

Fig. 2 Frontier molecular orbitals of YO.

the $X^2\Sigma^+$, $A^2\Pi$, $A'^2\Delta$, and $B^2\Sigma^+$ states of YO comprise the same closed-shell cationic configuration augmented with an additional unpaired electron occupying the valence 1σ, 1π, 1δ, and 2σ orbitals, respectively. Since the closed-shell configuration is stable, response theories using the closed-shell configuration as the reference and adding one electron to obtain the target states, *e.g.*, the equation-of-motion electron attachment coupled cluster (EOMEA-CC)[68] methods, are expected to provide balanced descriptions for these states. To investigate the accuracy of EOMEA-CC methods for the present application, we have carried out EOMEA-CC singles and doubles (CCSD) and singles doubles triples (CCSDT) calculations for the equilibrium geometries and vibrational frequencies of these four electronic states of YO. The EOMEA-CCSDT calculations have used the recent efficient implementation of EOM-CCSDT for excitation energies within the CFOUR program[69] together with the continuum-orbital trick[70] for accessing electron attached states. The scalar-relativistic effects have been taken into account using the spin-free exact two-component theory in its one-electron variant (SFX2C-1e)[65,71,72] unless otherwise specified. Perturbative treatment of spin–orbit coupling has been performed using spin–orbit integrals of the SFX2C-1e atomic mean-field (AMF) spin–orbit approach[73] and spin–orbit coupling matrix elements computed using the EOM-CCSD expectation-value formulation,[74,75] hereby taking the SFX2C-1e wavefunctions as the zeroth-order wavefunctions.[76] In this way, scalar-relativistic contributions to both the unperturbed states and the spin–orbit

integrals have been taken into account. This perturbative scheme has recently been shown to provide accurate spectroscopic parameters for the ThO^+ molecule,[73] which has an electronic structure similar to YO.

Unrestricted Hartree–Fock (UHF) based coupled-cluster singles doubles augmented with a noniterative triples [CCSD(T)][77,78] calculations have also been performed for the $X^2\Sigma^+$, $A^2\Pi$, and $A'^2\Delta$ states, which are the lowest electronic states in the corresponding irreducible representations. We have also carried out CCSD(T) calculations with non-perturbative treatment of spin–orbit coupling [SO-CCSD(T)][79] using the X2C scheme[72,80,81] and the corresponding AMF approach[82] for the $X^2\Sigma_{1/2}^+$, $A'^2\Delta_{3/2}$, and $A'^2\Delta_{5/2}$ states to obtain benchmark results for treatment of both spin–orbit coupling and electron correlation. These CCSD(T) calculations directly optimize the wavefunctions for the targeted states, and thus are expected to provide more accurate energies and properties than EOM-CC calculations when a similar level of truncation for the cluster expansion is applied. On the other hand, it should be noted that the EOM-CC methods are more flexible than the UHF-CC methods, especially for states that are not the lowest in an irreducible representation. Although we have converged UHF-CCSD(T) calculations for the $B^2\Sigma^+$ state as well as SO-CCSD(T) calculations for the $A^2\Pi_{1/2}$ and $A^2\Pi_{3/2}$ states in the vicinity of the equilibrium structures by using a maximum-overlap method (MOM),[83] convergence difficulties have been encountered for SO-CCSD(T) calculations of the $B^2\Sigma_{1/2}^+$ state.

The contraction coefficients of standard basis sets have been constructed for scalar-relativistic calculations. In the present study, we have used basis sets in the fully uncontracted form to ensure sufficient degrees of freedom for accurately accounting for both scalar-relativistic and spin–orbit effects. The set of primitive s-, p-, d-functions of the ANO-RCC basis set for yttrium[84] are augmented with correlating functions of cc-pCVTZ and cc-pCVQZ basis sets[85] to form TZ and QZ sets for yttrium. The uncontracted correlation consistent cc-pCVTZ and cc-pCVQZ basis sets of oxygen have been used and are denoted as TZ and QZ sets for oxygen.[86] Virtual orbitals with orbital energies greater than 1000 Hartree have been kept frozen in all CC calculations.

For each scheme of electronic-structure calculations, the local potential energy curves (PECs) have been scanned and fitted into sixth-order polynomial functions. Equilibrium bond lengths, harmonic vibrational frequencies, and anharmonic constants were obtained using these force constants and second-order vibrational perturbation theory.[87] More extensive calculations of PECs in the range of bond lengths [1.55 Å, 2.20 Å] covering around 10 000 cm^{-1} above the energies of the equilibrium geometries have also been performed for EOM-CC calculations. These computed energies have been fitted into tenth-order polynomials to reproduce the energies in this region faithfully. These *ab initio* PECs (documented in the ESI†) have been used for discrete variable representation (DVR)[88] calculations to obtain vibrational wavefunctions, energy levels, and Franck–Condon factors. DVR calculations have also been carried out using harmonic and Morse potentials with spectroscopic parameters including bond lengths, harmonic frequencies, and anharmonic constants obtained from *ab initio* calculations or experiments to test how the forms of PECs affect the computed Franck–Condon factors.

III. Results and discussions

A. Spin–orbit mixing and electronic transition dipole moments

The compositions of the $X^2\Sigma_{1/2}^+$, $A^2\Pi_{1/2}$, $A^2\Pi_{3/2}$, $A'^2\Delta_{3/2}$, $A'^2\Delta_{5/2}$, and $B^2\Sigma_{1/2}^+$ wavefunctions in terms of scalar-relativistic wavefunctions in the bond length of 1.8 Å have been obtained by diagonalizing the effective Hamiltonian (Table 1) and summarized in Table 2. The spin–orbit mixing between these scalar-relativistic wavefunctions is in general small, *e.g.*, the $A'^2\Delta_{3/2}$ state has a contribution of less than 0.1% from the $^2\Pi$ wavefunction (an expansion coefficient of *ca.* 0.03). Importantly, the $^2\Pi$–$^2\Delta$ spin–orbit mixing obtained in the present calculations is substantially smaller than the value reported in ref. 53 calculated using the spin–orbit coupling strength of yttrium 4d orbitals. This discrepancy can be attributed to that the $^2\pi$ orbitals are dominated by

Table 1 The effective Hamiltonian (cm^{-1}) diagonalized to obtain the low-lying spin–orbit-coupled states of YO in the bond length of 1.8 Å. Spin–orbit matrix elements (the off-diagonal elements) have been calculated using the SFX2C-1e EOM-CCSD transition density matrices and the SFX2C-1e AMF spin–orbit integrals, while the scalar-relativistic energies (the diagonal elements) are the SFX2C-1e-CCSD(T)/∞Z values

	$X^2\Sigma^+\left(m_s=\frac{1}{2}\right)$	$A^2\Pi_y\left(m_s=-\frac{1}{2}\right)$	$A^2\Pi_x\left(m_s=-\frac{1}{2}\right)$	$A'^2\Delta_{xy}\left(m_s=\frac{1}{2}\right)$	$A'^2\Delta_{2z^2-x^2-y^2}\left(m_s=\frac{1}{2}\right)$	$B^2\Sigma^+\left(m_s=\frac{1}{2}\right)$
$X^2\Sigma^+\left(m_s=\frac{1}{2}\right)$	0	−87.8i	87.8	0	0	0
$A^2\Pi_y\left(m_s=-\frac{1}{2}\right)$	89.1i	16544.7	−203.3i	−27.5	27.5i	−203.7i
$A^2\Pi_x\left(m_s=-\frac{1}{2}\right)$	89.1	203.3i	16544.7	−27.5i	−27.5	−203.7
$A'^2\Delta_{xy}\left(m_s=\frac{1}{2}\right)$	0	−26.1	26.1i	14651.2	140.3i	0
$A'^2\Delta_{2z^2-x^2-y^2}\left(m_s=\frac{1}{2}\right)$	0	−26.1i	−26.1	−140.3i	14651.2	0
$2B^2\Sigma^+\left(m_s=\frac{1}{2}\right)$	0	206.1i	−206.1	0	0	20999.9

Table 2 Combination coefficients of scalar-relativistic wavefunctions to compose the spin–orbit-coupled wavefunctions obtained by diagonalizing the effective Hamiltonian in Table 1

	$X^2\Sigma^+$	$A^2\Pi$	$A'^2\Delta$	$B^2\Sigma^+$
$X^2\Sigma_{1/2}^+$	0.99997	0.00771	0	0.0001
$A'^2\Delta_{3/2}$	0	0.02454	0.99970	0
$A'^2\Delta_{5/2}$	0	0	1.0	0
$A^2\Pi_{1/2}$	0.00760	0.99803	0	0.06221
$A^2\Pi_{3/2}$	0	0.99973	0.02334	0
$B^2\Sigma_{1/2}^+$	0.00036	0.06150	0	0.99811

yttrium $5p_{\pm1}$ contributions with only small contributions from $4d_{\pm1}$ orbitals (Fig. 1). Note that yttrium atomic spin–orbit interaction directly couples $4d_{\pm2}$ with $4d_{\pm1}$ but not with $5p_{\pm1}$. Therefore, as shown in Table 1, the spin–orbit matrix elements between the $^2\Pi$ and $^2\Delta$ wavefunctions amount to less than 30 cm^{-1}, one order of magnitude smaller than those between $^2\Delta_{xz}$ and $^2\Delta_{yz}$ wavefunctions. The small $^2\Pi$ and $^2\Delta$ spin–orbit mixing has important implications for the lifetime of the $A'^2\Delta$ state and the transition intensities of nominally dipole forbidden $A'^2\Delta \leftrightarrow X^2\Sigma$ and $B^2\Sigma \leftrightarrow A'^2\Delta$ transitions, as detailed below.

Computed electronic transition dipole moments between scalar-relativistic wavefunctions as summarized in Table 3 compare reasonably well with state-averaged complete active space self-consistent-field/multireference configuration interaction (CASSCF/MRCI) results reported in ref. 89. The present EOM-CCSD values of 2.11 a.u., 1.66 a.u., 0.10 a.u., and 1.06 a.u. for the $A^2\Pi \leftrightarrow X^2\Sigma^+$, $B^2\Sigma \leftrightarrow X^2\Sigma^+$, $B^2\Sigma^+ \leftrightarrow A^2\Pi$, $A^2\Pi \leftrightarrow A'^2\Delta$ transitions are consistent with corresponding CASSCF/MRCI values of 2.28 a.u., 1.84 a.u., 0.03 a.u., and 1.25 a.u. The transition dipole moments for dipole-allowed transitions between spin–orbit-coupled stated including the $A^2\Pi_{1/2} \leftrightarrow X^2\Sigma_{1/2}^+$, $B^2\Sigma_{1/2}^+ \leftrightarrow X^2\Sigma_{1/2}^+$, and $A^2\Pi_{1/2} \leftrightarrow A'^2\Delta_{3/2}$ transitions largely derive from the corresponding values between scalar-relativistic wavefunctions. As shown in Table 5, the lifetime values of 26 ns and 24 ns for the $A^2\Pi_{1/2}$ and $A^2\Pi_{3/2}$ states obtained using the Einstein *A* coefficients in Table 4 compare favorably with experimental values of 33 ns and 30 ns.[51] The computed lifetime of *ca.* 20 ns for the $B^2\Sigma_{1/2}^+$ state is similar to those of the $A^2\Pi$ states. The transition moment for the $A^2\Pi_{1/2} \leftrightarrow A'^2\Delta_{3/2}$ transition is of similar magnitude to that of the $B^2\Sigma_{1/2}^+ \leftrightarrow X^2\Sigma_{1/2}^+$ transition. Owing to the much smaller transition energy, the spontaneous decay rate from $A^2\Pi_{1/2}$ to $A'^2\Delta_{3/2}$ is three orders of magnitude lower than that from $A^2\Pi_{1/2}$ to $X^2\Sigma_{1/2}^+$. The computed branching ratio of 6×10^{-4} for $A^2\Pi_{1/2} \rightarrow A'^2\Delta_{3/2}$ is in reasonable agreement with the value of 3×10^{-4} reported in ref. 46.

Table 3 SFX2C-1e-EOM-CCSD transition dipole moments (a.u.) between scalar-relativistic wavefunctions as well as the dipole moments of the scalar-relativistic wavefunctions computed at the bond length of 1.8 Å using the TZ basis sets

	$X^2\Sigma^+$	$A^2\Pi_y$	$A^2\Pi_x$	$A'^2\Delta_{xy}$	$A'^2\Delta_{2z^2-x^2-y^2}$	$B^2\Sigma^+$
$X^2\Sigma^+$	1.87	−2.11	−2.11	0	0	−1.66
$A^2\Pi_y$	−2.10	1.59	0	1.06	−1.06	0.10
$A^2\Pi_x$	−2.10	0	1.59	1.06	1.06	0.10
$A'^2\Delta_{xy}$	0	1.07	1.07	3.07	0	0
$A'^2\Delta_{2z^2-x^2-y^2}$	0	−1.07	1.07	0	3.07	0
$B^2\Sigma^+$	−1.68	0.07	0.07	0	0	0.78

Table 4 The square of electronic transition dipole moments, $|TDM|^2$, and the oscillator strengths for transitions between spin–orbit-coupled wavefunctions computed at the bond length of 1.8 Å. The Einstein *A* coefficients for the corresponding spontaneous emission are also presented

	$\lvert TDM\rvert^2$ (a.u.)	Oscillator strength (a.u.)	Einstein *A* coefficient (s^{-1})
$A^2\Pi_{1/2,\pm1/2} \rightarrow X^2\Sigma_{1/2,\pm1/2}^+$	4.43	2.19×10^{-1}	3.90×10^{7}
$A^2\Pi_{1/2,\pm1/2} \rightarrow X^2\Sigma_{1/2,\mp1/2}^+$	0.01	5.14×10^{-4}	9.13×10^{4}
$A^2\Pi_{3/2,\pm3/2} \rightarrow X^2\Sigma_{1/2,\pm1/2}^+$	4.44	2.26×10^{-1}	4.23×10^{7}
$A'^2\Delta_{3/2,\pm3/2} \rightarrow X^2\Sigma_{1/2,\pm1/2}^+$	4.0×10^{-3}	1.77×10^{-4}	2.50×10^{4}
$B^2\Sigma_{1/2,\pm1/2}^+ \rightarrow X^2\Sigma_{1/2,\pm1/2}^+$	2.76	1.74×10^{-1}	5.02×10^{7}
$B^2\Sigma_{1/2,1/2}^+ \rightarrow X^2\Sigma_{1/2,\mp1/2}^+$	1.7×10^{-2}	1.06×10^{-3}	3.06×10^{5}
$A^2\Pi_{1/2,\pm1/2} \rightarrow A'^2\Delta_{3/2,\pm3/2}$	2.26	1.23×10^{-2}	2.61×10^{4}
$A^2\Pi_{3/2,\pm3/2} \rightarrow A'^2\Delta_{3/2,\pm3/2}$	1.0×10^{-3}	7.16×10^{-6}	2.34×10^{1}
$B^2\Sigma_{1/2,\pm1/2}^+ \rightarrow A'^2\Delta_{3/2,\pm3/2}$	8.2×10^{-3}	1.56×10^{-4}	4.08×10^{3}
$A^2\Pi_{3/2,\pm3/2} \rightarrow A'^2\Delta_{5/2,\pm5/2}$	2.27	1.30×10^{-2}	3.04×10^{4}
$B^2\Sigma_{1/2,\pm1/2}^+ \rightarrow A^2\Pi_{1/2,\pm1/2}$	7.2×10^{-3}	9.74×10^{-5}	1.30×10^{3}
$B^2\Sigma_{1/2,\pm1/2}^+ \rightarrow A^2\Pi_{1/2,\mp1/2}$	2.4×10^{-3}	3.22×10^{-5}	4.31×10^{2}
$B^2\Sigma_{1/2,\pm1/2}^+ \rightarrow A^2\Pi_{3/2,\pm3/2}$	7.6×10^{-3}	9.30×10^{-5}	1.02×10^{3}

Table 5 Computed and measured spontaneous emission lifetimes

	Computed	Measured
$A^2\Pi_{1/2}$	26 ns	33 ns[51]
$A^2\Pi_{3/2}$	24 ns	30 ns[51]
$A'^2\Delta_{3/2}$	40 μs	23(2) μs (this work)
$B^2\Sigma_{1/2}$	20 ns	—

The $A'^2\Delta_{3/2} \leftrightarrow X^2\Sigma_{1/2}^+$ and $B^2\Sigma_{1/2}^+ \leftrightarrow A'^2\Delta_{3/2}$ transitions are nominally dipole forbidden and borrow intensities entirely through spin–orbit mixing. As shown in Table 4, the transition moment for the $A'^2\Delta_{3/2} \leftrightarrow X^2\Sigma_{1/2}^+$ transition is three order of magnitude smaller than that of the dipole-allowed $A^2\Pi_{1/2} \leftrightarrow X^2\Sigma_{1/2}^+$ transition. This leads to a value of 40 μs for the spontaneous decay lifetime of the $A'^2\Delta_{3/2}$ state, around 1500 times longer than that of the $A^2\Pi_{1/2}$ state. This computed lifetime for the $A'^2\Delta_{3/2}$ state is in good agreement with the measured value of 23(2) μs presented in Section II-A. The $B^2\Sigma_{1/2}^+ \leftrightarrow A'^2\Delta_{3/2}$ transition has an oscillator strength of similar magnitude to that of the $A'^2\Delta_{3/2} \leftrightarrow X^2\Sigma_{1/2}^+$ transition. Finally, since the unpaired electrons in the $X^2\Sigma^+$, $A^2\Pi$, and $B^2\Sigma^+$ states are dominated by yttrium 5s, $5p_x/5p_y$, and $5p_z$ orbitals, respectively, $B^2\Sigma_{1/2}^+ \leftrightarrow A^2\Pi_{1/2}$ transition possesses a much smaller transition dipole moment (25 times smaller) than that of the $B^2\Sigma_{1/2}^+ \leftrightarrow X^2\Sigma_{1/2}^+$ transition. Consequently, the oscillator strength of this transition is only about the same magnitude as those of dipole-forbidden transitions.

B. Benchmark calculations of molecular parameters and Franck–Condon factors

1. Equilibrium geometries, harmonic frequencies, and term energies. Since Franck–Condon factors (FCFs) involving low-lying vibrational states are largely determined by the local potential energy curves (PECs), we first focus on structural parameters such as equilibrium bond lengths and vibrational

Table 6 Equilibrium bond lengths (Å) for low-lying electronic states of YO. "lc" and "sc" refer to freezing 15 and 5 core orbitals in coupled-cluster calculations, respectively

	$X^2\Sigma^+$	$A'^2\Delta$ ($^2\Delta_{3/2}/^2\Delta_{5/2}$)	$A^2\Pi$ ($A^2\Pi_{1/2}/A^2\Pi_{3/2}$)	$B^2\Sigma^+$
EOM-CCSD/TZ/lc	1.7813	1.8038	1.7838	1.8125
EOM-CCSDT/TZ/lc	1.7979	1.8261	1.8006	1.8313
CCSD(T)/TZ/lc	1.7922	1.8184	1.7955	1.8262
EOM-CCSD/∞Z/sc + ΔT	1.7909	1.8198	1.7951	1.8252
EOM-CCSD/∞Z/sc + ΔT + ΔSO	1.7921	1.8212/1.8205	1.7968/1.7959	1.8263
SO-CCSD(T)/TZ/sc	1.7915	1.8180/1.8172	1.7951/1.7943	—
SO-CCSD(T)/QZ/sc	1.7883	1.8153/1.8144	1.7928/1.7921	—
SO-CCSD(T)/∞Z/sc	1.7859	1.8123/1.8115	1.7911/1.7904	—
Experiment	1.7875	1.8184	1.7936	1.8252

frequencies that characterize the local PECs. In general, EOM-CCSD provides qualitatively correct results, while the inclusion of triples contributions build the way to obtain accurate results. The triples corrections (the difference between EOM-CCSDT and EOM-CCSD, the first two rows in Tables 6 and 7) amount to around 0.02 Å for equilibrium bond lengths and around 50 cm^{-1} for harmonic frequencies. EOM-CCSD underestimates the bond lengths and overestimate harmonic frequencies for all the electronic states studied here. The basis-set and core-correlation effects are smaller, *i.e.*, around 0.005 Å for the bond lengths and a few cm^{-1} for harmonic frequencies. Spin–orbit corrections (the difference between the fourth and fifth rows in Tables 6 and 7) amount to around 0.001 Å for bond lengths and a few cm^{-1} for harmonic frequencies. The deviations between the best EOM-CC results (the rows "EOM-CCSD/∞Z/sc + ΔT + ΔSO" in Tables 6 and 7) and experimental values are below 0.005 Å for bond lengths and 15 cm^{-1} for harmonic frequencies.

As shown in Tables 6 and 7, SO-CCSD(T) bond lengths are as accurate as the best EOM values, while SO-CCSD(T) harmonic frequencies agree with experiment even more closely. Namely, SO-CCSD(T) harmonic frequencies are around 5 cm^{-1} higher than the corresponding experimental values, while the EOM values are 10 cm^{-1} lower than the experiments. A notable exception is that, although it is also 15 cm^{-1} higher than the EOM values, CCSD(T) harmonic frequency for $B^2\Sigma^+$ is more than 20 cm^{-1} greater than the experimental value. This might be due to a perturbing electronic state nearly degenerate to vibrational excited states of $B^2\Sigma^+$[56] and seems worth further investigation. The perturbing electronic state is not expected to have significant effects on the present calculations of Franck–Condon factors, which only include vibrational ground state of $B^2\Sigma^+$. On the other hand, in future work it might be worthwhile to analyze perturbations that couple these electronic states in more detail.[90–92] Note that CCSD(T) features a noniterative triples correction to CCSD with a cost of a single step that scales as the seventh power of the system size, while the cost of CCSDT scales as the eighth power of the system size for each CC iteration. Therefore, CCSD(T) appears to be a more efficient approach for the present purpose of obtaining accurate spectroscopic parameters for YO. The SO effects obtained from SO-CCSD(T) calculations are consistent with those obtained from perturbative SO calculations, *e.g.*, the spin–orbit splittings of bond lengths and harmonic frequencies amount to around 0.001 Å and 1 cm^{-1}.

Unlike in calculations of bond lengths and harmonic frequencies, basis-set effects play an important role in calculations of term energies. Since the $X^2\Sigma$ and $A'^2\Delta$ states possess quite different electronic orbital angular momenta, differential basis-set effects on the term energy of $A'^2\Delta$ are significant. As shown in Table 8, the remaining basis-set effects for the term energies of the $A'^2\Delta$ states obtained using the TZ basis amount to more than 600 cm^{-1}. It thus is necessary to perform basis-set extrapolation[93] to estimate the basis-set-limit values to obtain accurate results. CCSD(T) appear to be more accurate than EOM-CCSDT for term energies, *e.g.*, EOM-CCSDT term

Table 7 Harmonic vibrational frequencies (cm^{-1}) for low-lying electronic states of YO. "lc" and "sc" refer to freezing 15 and 5 core orbitals in coupled-cluster calculations, respectively

	$X^2\Sigma^+$	$A'^2\Delta$ ($^2\Delta_{3/2}/^2\Delta_{5/2}$)	$A^2\Pi$ ($A^2\Pi_{1/2}/A^2\Pi_{3/2}$)	$B^2\Sigma^+$
EOM-CCSD/TZ/lc	893.8	837.1	860.1	817.8
EOM-CCSDT/TZ/lc	851.6	784.9	818.4	775.2
CCSD(T)/TZ/lc	864.2	797.6	829.1	788.3
EOM-CCSD/∞Z/sc + ΔT	853.5	785.7	815.9	774.6
EOM-CCSD/∞Z/sc + ΔT + ΔSO	852.3	784.5/785.4	813.8/814.5	773.1
SO-CCSD(T)/TZ/sc	866.0	798.7/799.9	830.7/831.5	—
SO-CCSD(T)/QZ/sc	866.0	798.9/800.2	827.9/828.6	—
SO-CCSD(T)/∞Z/sc	866.0	799.1/800.3	826.5/825.9	—
Experiment	862.0	794.6	821.5	758.7/765.5

Table 8 Equilibrium term energies (cm^{-1}) for low-lying electronic states of YO. "lc" and "sc" refer to freezing 15 and 5 core orbitals in coupled-cluster calculations, respectively

	$X^2\Sigma^+$	$A'^2\Delta$ ($^2\Delta_{3/2}/^2\Delta_{5/2}$)	$A^2\Pi$ ($A^2\Pi_{1/2}/A^2\Pi_{3/2}$)	$B^2\Sigma^+$
EOM-CCSD/TZ/lc	0	15386.5	16693.8	21620.7
EOM-CCSDT/TZ/lc	0	14956.5	16706.7	21265.5
CCSD(T)/TZ/lc	0	15149.9	16589.5	21020.4
EOM-CCSD/∞Z/sc + ΔT	0	14486.9	16659.5	21169.6
EOM-CCSD/∞Z/sc + ΔT + ΔSO	0	14344.7/14629.8	16441.2/16864.5	21189.4
SO-CCSD(T)/TZ/sc	0	15144.5/15469.7	16417.3/16846.6	—
SO-CCSD(T)/QZ/sc	0	14766.3/15097.0	16369.4/16802.0	—
SO-CCSD(T)/∞Z/sc	0	14491.0/14825.7	16335.6/16770.5	—
Experiment	0	14531.2/14870.4	16315.8/16746.8	20793.33

Table 9 Variation of calculated FCFs for the $A^2\Pi(0) \rightarrow X^2\Sigma^+(\nu)$, $B^2\Sigma^+(0) \rightarrow X^2\Sigma^+(\nu)$, and $A'^2\Delta(0) \rightarrow X^2\Sigma^+(\nu)$ transitions with respect to the shift of bond-length differences $R_e(A^2\Pi) - R_e(X^2\Sigma^+)$, $R_e(B^2\Sigma^+) - R_e(X^2\Sigma^+)$, and $R_e(A'^2\Delta) - R_e(X^2\Sigma^+)$. The origin refers to the use of EOM-CCSD/∞Z/sc + ΔT potential energy curves. FCFs greater than 0.001% are explicitly given

		Shifts of bond-length difference (Å)					
Transitions	ν	−0.003	0.000	0.003	0.005	0.010	0.020
$A^2\Pi(0) \rightarrow X^2\Sigma(\nu)$	0	99.938%	99.643%	99.049%	98.491%	96.541%	90.459%
	1	0.039%	0.338%	0.928%	1.480%	3.392%	9.181%
	2	0.022%	0.020%	0.023%	0.029%	0.066%	0.353%
	3	<0.001%	<0.001%	<0.001%	<0.001%	0.001%	0.007%
$B^2\Sigma(0) \rightarrow X^2\Sigma(\nu)$	0	84.897%	82.195%	79.345%	77.374%	72.244%	61.460%
	1	13.848%	16.127%	18.450%	20.005%	23.842%	30.803%
	2	1.185%	1.575%	2.055%	2.429%	3.571%	6.786%
	3	0.066%	0.098%	0.143%	0.182%	0.322%	0.873%
	4	0.003%	0.004%	0.007%	0.009%	0.020%	0.074%
	5	<0.001%	<0.001%	<0.001%	<0.001%	0.001%	0.004%
$A'^2\Delta(0) \rightarrow X^2\Sigma(\nu)$	0	89.306%	86.907%	84.323%	82.508%	77.690%	67.207%
	1	10.058%	12.198%	14.443%	15.981%	19.895%	27.477%
	2	0.612%	0.857%	1.174%	1.432%	2.258%	4.810%
	3	0.023%	0.037%	0.058%	0.077%	0.149%	0.476%
	4	0.001%	0.001%	0.002%	0.003%	0.006%	0.029%
	5	<0.001%	<0.001%	<0.001%	<0.001%	<0.001%	0.001%

energies of the $A'^2\Delta$ states appear to be 200 cm^{-1} too high, while the SO-CCSD(T) ones agree with the experimental values to within 50 cm^{-1}. Perturbative spin–orbit calculations have obtained values of 285 cm^{-1} and 423 cm^{-1} for the spin–orbit splittings of the $A'^2\Delta$ and $A^2\Pi$ states, which compare reasonably well with experimental values of 339 cm^{-1} and 431 cm^{-1}. SO-CCSD(T) provides more accurate spin–orbit splittings, which agree with experimental values to within 5 cm^{-1}. Computed term energies are obviously less accurate than experimental values obtained from using high resolution laser spectroscopy. On the other hand, for electronic states in absence of experimental measurements, *e.g.*, the $A'^2\Delta$ state of BaF or RaF, one may speculate that electronic-structure calculations may provide useful estimate for energy levels to facilitate experimental search for these states.

2. Franck–Condon factors. As vibrational overlap integrals, Franck–Condon factors (FCFs) are expected to be sensitive to the difference between the equilibrium bond lengths of two electronic states. The variation of computed FCFs with respect to bond-length differences is demonstrated in Table 9 with calculations using the same PECs with shifted equilibrium bond lengths. The absolute values of individual FCFs are very sensitive to the variation of bond-length differences, with an approximate linear dependence. For example, a shift of the bond-length difference by 0.005 (or 0.01) Å leads to a change of the FCF for the $B^2\Sigma(0) \rightarrow X^2\Sigma(0)$ transition by around 5% (or 10%). On the other hand, the sum of FCFs up to a certain vibrational level is less sensitive to the change of bond-length difference. For example, the sum of FCFs for the $B^2\Sigma^+(0) \rightarrow X^2\Sigma^+(\nu)$ transitions with ν = 0–3 (ν = 0–4) saturates to 99.99% (99.999%) for all calculations with a shift of bond-length difference less than 0.01 Å. In general it seems necessary to have bond-length difference accurate to within 0.01 Å to obtain qualitatively correct results for FCFs and to within 0.003 Å to obtain quantitative results. We mention that, as show in ESI,† the dependence of computed FCFs with respect to harmonic frequencies is less pronounced.

As discussed in the previous section, the EOM-CCSD equilibrium bond lengths differ from experimental values by more than 0.01 Å. One may expect significant errors in computed bond-length differences and FCFs. However, it should be noted that EOM-CCSD consistently overestimates the equilibrium bond lengths for all electronic states studied here; the errors

Table 10 Franck–Condon factors calculated using EOM-CC potential energy curves. In the last column with spin–orbit coupling included, $X^2\Sigma^+$, $B^2\Sigma^+$, $A^2\Pi$, and $A'^2\Delta$ refer to $X^2\Sigma_{1/2}{}^+$, $B^2\Sigma_{1/2}{}^+$, $A^2\Pi_{1/2}$, and $A'^2\Delta_{3/2}$, respectively. FCFs greater than 0.001% are explicitly given

Transitions	ν	CCSD/TZ/lc (%)	CCSDT/TZ/lc	CCSD/∞Z/lc + ΔT (%)	CCSD/∞Z/sc + ΔT (%)	CCSD/∞Z/sc + T + ΔSO (%)
$A^2\Pi(0) \rightarrow X^2\Sigma^+(\nu)$	0	99.851	99.836	99.600	99.643	99.563
	1	0.135	0.149	0.380	0.338	0.416
	2	0.014	0.015	0.020	0.020	0.020
$B^2\Sigma^+(0) \rightarrow X^2\Sigma^+(\nu)$	0	84.296	83.034	81.885	82.195	82.411
	1	14.367	15.444	16.372	16.127	15.954
	2	1.262	1.434	1.633	1.575	1.536
	3	0.072	0.085	0.104	0.098	0.094
	4	0.003	0.004	0.005	0.004	0.004
$A'^2\Delta(0) \rightarrow X^2\Sigma^+(\nu)$	0	91.389	87.518	86.805	86.907	86.600
	1	8.210	11.661	12.287	12.198	12.464
	2	0.389	0.787	0.869	0.857	0.895
	3	0.011	0.033	0.038	0.037	0.040
	4	<0.001	0.001	0.001	0.001	0.001

for EOM-CCSD bond-length differences thus are less than 0.01 Å. Consequently, while EOM-CCSD tends to overestimate the diagonal FCFs, EOM-CCSD results are in general robust and qualitatively correct. As shown in Table 10, the deviations of the EOM-CCSD result from those of EOM-CCSDT amount to 1% for the FCF of the $B^2\Sigma^+(0) \rightarrow X^2\Sigma^+(0)$ transition and to 4% for the FCF of the $A'^2\Delta(0) \rightarrow X^2\Sigma^+(0)$ transition. The vibrational transitions required to saturate the sum of $A^2\Pi(0) \rightarrow X^2\Sigma^+(\nu)$ FCFs to more than 99.999% are both $\nu = 0$–2 for EOM-CCSD and EOM-CCSDT calculations. We mention that enlargement of basis sets reduces the bond lengths for all electronic states and has small effects on bond-length differences and hence FCFs (shown as the differences between the second and third columns of Table 10). The effects of core correlation and spin–orbit coupling appear to be even smaller.

The forms of the potential energy functions seem to play a minor role in calculations of FCFs. While the use of harmonic approximation could introduce significant errors for transitions to higher vibrational levels (see the difference between the first and second columns of Table 11), the results obtained using Morse potentials agree closely with those obtained using *ab initio* potentials, provided they share the same equilibrium bond lengths, harmonic frequencies, and anharmonic constants. The first and third columns of Table 11 respectively show FCFs obtained using the best EOM potential and the Morse potential with the same spectroscopic parameters. The differences between these FCFs are essentially negligible. In contrast, the results obtained using EOM and experimental parameters (columns 3 and 4 in Table 11) differ more substantially. When the EOM potential is shifted to match the experimental equilibrium bond length (the last column of Table 11), the results agree very well with those obtained using Morse potentials with experimental parameters. Since the semiempirical Morse potentials with accurate spectroscopic parameters are capable of providing accurate FCFs, a useful practical computational strategy is to obtain spectroscopic parameters from relativistic CCSD(T) or EOM-CC calculations and then calculate FCFs using Morse potentials built with these parameters.

Table 11 Calculated FCFs for transition using a variety of potential energy curves. "EOM" refers to using *ab initio* EOM-CCSD/∞Z/sc + ΔT potential energy curves. "Harmonic (EOM)" and "Morse (EOM)" denote the use of harmonic and Morse potentials with *ab initio* spectroscopic parameters. "Morse (Exp.)" refers to using a Morse potential with experimental parameters. "EOM (shifted)" refers to the use of the *ab initio* potential shifted to match the experimental equilibrium bond length. FCFs greater than 0.001% are explicitly given

Transitions	ν	EOM (%)	Harmonic (EOM) (%)	Morse (EOM) (%)	Morse (Exp.) (%)	EOM (shifted) (%)
$A^2\Pi(0) \rightarrow X^2\Sigma(\nu)$	0	99.643	99.679	99.648	99.261	99.301
	1	0.338	0.288	0.333	0.715	0.678
	2	0.020	0.032	0.019	0.024	0.021
$B^2\Sigma(0) \rightarrow X^2\Sigma(\nu)$	0	82.195	82.423	82.142	76.584	77.174
	1	16.127	15.068	16.176	20.345	20.160
	2	1.575	2.204	1.579	2.784	2.469
	3	0.098	0.271	0.098	0.266	0.187
	4	0.004	0.030	0.004	0.020	0.010
	5	<0.001	0.003	<0.001	0.001	<0.001
$A'^2\Delta(0) \rightarrow X^2\Sigma(\nu)$	0	86.907	87.087	86.912	85.018	85.204
	1	12.198	11.472	12.197	13.879	13.685
	2	0.857	1.305	0.853	1.053	1.060
	3	0.037	0.125	0.037	0.049	0.050
	4	0.001	0.011	0.001	0.001	0.002
	5	<0.001	0.001	<0.001	<0.001	<0.001

C. Prospects for enhancing laser cooling efficiencies for YO

1. An alternative scheme for addressing the leakage through the $A'^2\Delta_{3/2}$ state. Laser cooling of molecules typically requires scattering of $\sim 10^5$ photons. The YO molecules with an initial speed of 100 m s^{-1} have been reported to be slowed to ~ 5 m s^{-1},[47] captured by a magneto-optical trap,[48] and laser cooled to 4 μK.[94] The transition $A^2\Pi_{1/2} \leftrightarrow X^2\Sigma_{1/2}^+$ is employed as the optical cycling transition and only two vibrational repumpers are required to scatter enough number of photons for cooling. This observation is consistent with the computational results for FCFs as shown in Table 11. However, except directly decaying to $X^2\Sigma^+$, YO molecules in the $A^2\Pi_{1/2}$ state also leak to $A'^2\Delta_{3/2}$ with a branching ratio on the order of 10^{-4} (6×10^{-4} as derived from Table 4 and 3×10^{-4} as reported in ref. 47), and subsequently decay to $X^2\Sigma_{1/2}^+$ from $A'^2\Delta_{3/2}$. This is a three-photon process and the molecules end up in rotational states with opposite parity compared with the initial $X^2\Sigma_{1/2}^+$ states in the $A^2\Pi_{1/2} \leftrightarrow X^2\Sigma_{1/2}^+$ cycle. Separate lasers and microwaves are required to repump these dark states in various rotational states back to the initial states, as demonstrated in ref. 47 and 48. However, the FCFs of the $A'^2\Delta_{3/2} \leftrightarrow X^2\Sigma_{1/2}$ transition are not highly diagonal with the FCF of the $A'^2\Delta_{3/2}(0) \leftrightarrow X^2\Sigma_{1/2}^+(0)$ transition being less than 90% (Table 11). More than one vibrational states might need to be repumped to enable scattering of 10^5 photons, which substantially complicates the repumping scheme.

We present here an alternative scheme to close the leakage through $A'^2\Delta_{3/2}$ by coupling $A'^2\Delta_{3/2}$ to $B^2\Sigma_{1/2}^+$. The normally dipole-forbidden transition $B^2\Sigma_{1/2}^+ \leftrightarrow A'^2\Delta_{3/2}$ borrows intensity from spin–orbit coupling and has a similar oscillator strength as $A'^2\Delta_{3/2} \leftrightarrow X^2\Sigma_{1/2}^+$ (Table 4). This transition has a saturation intensity of 0.19 μW cm^{-2}, and can be readily saturated using a laser at 1.602 μm. It reduces the probability for $A'^2\Delta_{3/2}$ to spontaneously decay to $X^2\Sigma_{1/2}$ by a factor of $\tau_{A'}/\tau_B \sim 10^3$, where $\tau_{A'}$ and τ_B are the lifetimes of $A'^2\Delta_{3/2}$ and $B^2\Sigma_{1/2}^+$, respectively. This suppression factor is high enough for us to ignore the direct decay from $A'^2\Delta_{3/2}$. The molecules in $B^2\Sigma^+$ subsequently decay to $A^2\Pi_{1/2}$ and $X^2\Sigma_{1/2}^+$. Note that the $B^2\Sigma_{1/2}^+ \leftrightarrow A^2\Pi_{1/2}$ transition possesses a very small transition dipole moment, 25 times smaller than that of the $B^2\Sigma_{1/2}^+ \leftrightarrow X^2\Sigma_{1/2}^+$ transition (Table 4). Consequently, the spontaneous decay rate of the former transition is four orders of magnitude smaller than that of the latter one, which indicates that a vast majority of the molecules in $B^2\Sigma_{1/2}^+$ decay directly to $X^2\Sigma_{1/2}^+$. This optical cycle involves $X^2\Sigma_{1/2}^+$, $A^2\Pi_{1/2}$, $A'^2\Delta_{3/2}$, and $B^2\Sigma_{1/2}^+$ states, forming a four-photon process, and preserves the parity of the states. Therefore, the molecules decay back to the same rotational states of $X^2\Sigma_{1/2}^+$ as those in the $A^2\Pi_{1/2} \leftrightarrow X^2\Sigma_{1/2}^+$ optical cycle.

2. Narrow-line cooling below recoil temperature. A cooling scheme using the narrow linewidth of the $A'^2\Delta_{3/2}$ state has been proposed and analyzed in detail in ref. 46. (For the transitions involved in this scheme, see Fig. 3 of ref. 46.) Since the $^2\Pi$–$^2\Delta$ spin–orbit mixing is significantly lower than previously reported and the linewidth of the $A'^2\Delta_{3/2}$ state is much narrower than that used in ref. 46, it would be of interest to update the analysis of the narrow-line cooling scheme. The Doppler temperature estimated using the measured lifetime of 23 μs for the $A'^2\Delta_{3/2}$ state is 160 nK, which is below the recoil temperature of 200 nK and more than one order of magnitude lower than the lowest temperature achieved so far for laser-cooled molecules.[94] We mention that the Doppler temperature estimated using the computed lifetime of 40 μs amounts to around 100 nK. Here we adopt the more conservative value of 160 nK in our discussion. This deep cooling can be applied following the gray molasses cooling, which is recently shown to be able to cool YO molecules to 4 μK.[94] According to the computed FCFs of the $A'^2\Delta_{3/2} \leftrightarrow X^2\Sigma_{1/2}^+$ transition (the last two columns of Table 11), repumping one vibrationally excited state forms an optical cycle containing around 99% vibrational branching. This enables $\sim$100 photon scatterings and might be enough for sub-recoil cooling.

The narrow linewidth of $A'^2\Delta_{3/2}$ makes it feasible to apply SWAP[95–97] cooling to YO molecules.[98] SWAP cooling relies on the time-ordered photon absorption and emission, and substantially reduces the number of photon scattering events required for cooling atoms or molecules. This technique has been recently demonstrated to cool Sr atoms[95,97] using a transition with a similar linewidth. Extending SWAP cooling to YO molecules could open up the possibility for laser cooling a large class of molecules with less diagonal FCFs.

It has been proposed to implement quantum gates with diatomic molecules by making use of the dipole–dipole interaction.[99,100] The rapid progress in creating ultracold molecules, either by association of ultracold atoms or by direct laser cooling of molecules, and loading them in an optical lattice[101] or an optical tweezer array[102] makes this perspective particularly appealing. Control of the molecular motion in the quantum regime is desirable for high gate fidelity.[100] However, due to the large tensor Stark shifts presented in molecules in an optical trap, it is challenging to apply the cooling techniques demonstrated for atoms, *e.g.*, Raman sideband cooling, to molecules.[103] This challenge can be overcome by using the narrow-line cooling, which has been demonstrated to be capable of cooling alkaline earth atoms[104–107] to ground state of motion in optical tweezers. Narrow-line cooling of YO molecules represents a simple method to control the molecular motion in the quantum regime, which paves the way for implementing quantum gates between dipolar molecules.

IV. Summary and outlook

Benchmark calculations for the electronic and vibrational structures of low-lying electronic states of YO are reported. Coupled-cluster methods, which offer accurate treatment of electron correlation around equilibrium structures, appear to be promising candidates for accurate calculations of Franck–Condon factors. In this context, accurate calculation of equilibrium structures seems of paramount importance. It would be of particular interest to extend the coupled-cluster techniques from molecules containing light elements[108,109] to heavy-metal containing molecules by including scalar-relativistic and spin–orbit effects to obtain highly accurate molecular structures.

A four-photon process comprising repumping from the $A'^2\Delta_{3/2}$ state to the $B^2\Sigma_{1/2}^+$ state is proposed to address leakage of the $A^2\Pi_{1/2} \leftrightarrow X^2\Sigma_{1/2}^+$ cycle through the $A'^2\Delta_{3/2}$ state. This scheme is supported by the computed electronic transition properties and Franck–Condon factors. Further, prospects of a narrow-line cooling scheme[46] using the $A'^2\Delta_{3/2}$ state have been updated using the computed transition properties and the measured lifetime of the $A'^2\Delta_{3/2}$ state. This narrow-line cooling scheme has the potential to bring YO molecules to sub-recoil temperature.

Conflicts of interest

There are no conflicts to declare.

Acknowledgements

The work at Johns Hopkins University was supported by the National Science Foundation, under grant no. PHY-1011794. Y. W. and S. D. are indebted to Jun Ye (Boulder) for stimulating discussions and generous supports. L. C. would like to thank Jinjun Liu (Louisville) and Nike Dattani for helpful discussions. All computations have been performed at the Maryland Advanced Research Computing Center.

References

1 L. D. Carr, D. DeMille, R. V. Krems and J. Ye, *New J. Phys.*, 2009, **11**, 55049.
2 L. R. Liu, J. D. Hood, Y. Yu, J. T. Zhang, N. R. Hutzler, T. Rosenband and K.-K. Ni, *Science*, 2018, **360**, 900–903.
3 L. Anderegg, L. W. Cheuk, Y. Bao, S. Burchesky, W. Ketterle, K.-K. Ni and J. M. Doyle, *Science*, 2019, **365**, 1156–1158.
4 M. T. Bell and T. P. Softley, *Mol. Phys.*, 2009, **107**, 99–132.
5 S. Ospelkaus, K.-K. Ni, D. Wang, M. H. G. de Miranda, B. Neyenhuis, G. Quéméner, P. S. Julienne, J. L. Bohn, D. S. Jin and J. Ye, *Science*, 2010, **327**, 853–857.
6 J. M. Hutson, *Science*, 2010, **327**, 788–789.
7 G. Quéméner and P. S. Julienne, *Chem. Rev.*, 2012, **112**, 4949–5011.
8 K.-K. Ni, S. Ospelkaus, M. H. G. de Miranda, A. Pe'er, B. Neyenhuis, J. J. Zirbel, S. Kotochigova, P. S. Julienne, D. S. Jin and J. Ye, *Science*, 2008, **322**, 231–235.
9 J. J. Hudson, B. E. Sauer, M. R. Tarbutt and E. A. Hinds, *Phys. Rev. Lett.*, 2002, **89**, 23003.
10 E. R. Meyer, J. L. Bohn and M. P. Deskevich, *Phys. Rev. A: At., Mol., Opt. Phys.*, 2006, **73**, 62108.
11 H. Loh, K. C. Cossel, M. C. Grau, K.-K. Ni, E. R. Meyer, J. L. Bohn, J. Ye and E. A. Cornell, *Science*, 2013, **342**, 1220–1222.
12 J. Baron, W. C. Campbell, D. DeMille, J. M. Doyle, G. Gabrielse, Y. V. Gurevich, P. W. Hess, N. R. Hutzler, E. Kirilov, I. Kozyryev, B. R. O'Leary, C. D. Panda, M. F. Parsons, E. S. Petrik, B. Spaun, A. C. Vutha and A. D. West, *Science*, 2014, **343**, 269–272.
13 V. Andreev, D. G. Ang, D. DeMille, J. M. Doyle, G. Gabrielse, J. Haefner, N. R. Hutzler, Z. Lasner, C. Meisenhelder, B. R. O'Leary, C. D. Panda, A. D. West, E. P. West, X. Wu and A. Collaboration, *Nature*, 2018, **562**, 355–360.
14 W. B. Cairncross, D. N. Gresh, M. Grau, K. C. Cossel, T. S. Roussy, Y. Ni, Y. Zhou, J. Ye and E. A. Cornell, *Phys. Rev. Lett.*, 2017, **119**, 153001.
15 I. Kozyryev and N. R. Hutzler, *Phys. Rev. Lett.*, 2017, **119**, 133002.
16 D. DeMille, J. M. Doyle and A. O. Sushkov, *Science*, 2017, **357**, 990–994.
17 W. B. Cairncross and J. Ye, *Nat. Rev. Phys.*, 2019, **1**, 510–521.
18 J. D. Weinstein, R. DeCarvalho, T. Guillet, B. Friedrich and J. M. Doyle, *Nature*, 1998, **395**, 148–150.
19 E. S. Shuman, J. F. Barry and D. DeMille, *Nature*, 2010, **467**, 820–823.
20 M. T. Hummon, M. Yeo, B. K. Stuhl, A. L. Collopy, Y. Xia and J. Ye, *Phys. Rev. Lett.*, 2013, **110**, 143001.
21 I. Kozyryev, L. Baum, K. Matsuda and J. M. Doyle, *ChemPhysChem*, 2016, **17**, 3641–3648.
22 I. Kozyryev, L. Baum, K. Matsuda, B. L. Augenbraun, L. Anderegg, A. P. Sedlack and J. M. Doyle, *Phys. Rev. Lett.*, 2017, **118**, 173201.
23 S. Truppe, H. J. Williams, M. Hambach, L. Caldwell, N. J. Fitch, E. A. Hinds, B. E. Sauer and M. R. Tarbutt, *Nat. Phys.*, 2017, **13**, 1173–1176.
24 L. Anderegg, B. L. Augenbraun, Y. Bao, S. Burchesky, L. W. Cheuk, W. Ketterle and J. M. Doyle, *Nat. Phys.*, 2018, **14**, 890–893.
25 J. Lim, J. R. Almond, M. A. Trigatzis, J. A. Devlin, N. J. Fitch, B. E. Sauer, M. R. Tarbutt and E. A. Hinds, *Phys. Rev. Lett.*, 2018, **120**, 123201.
26 B. L. Augenbraun, Z. D. Lasner, A. Frenett, H. Sawaoka, C. Miller, T. C. Steimle and J. M. Doyle, *New J. Phys.*, 2020, **22**, 22003.
27 B. L. Augenbraun, J. M. Doyle, T. Zelevinsky and I. Kozyryev, *Phys. Rev. X*, 2020, **10**, 31022.
28 I. Kozyryev, T. C. Steimle, P. Yu, D.-T. Nguyen and J. M. Doyle, *New J. Phys.*, 2019, **21**, 52002.
29 E. T. Mengesha, A. T. Le, T. C. Steimle, L. Cheng, C. Zhang, B. L. Augenbraun, Z. Lasner and J. Doyle, *J. Phys. Chem. A*, 2020, **124**, 3135–3148.
30 X. Zhuang, A. Le, T. C. Steimle, N. E. Bulleid, I. J. Smallman, R. J. Hendricks, S. M. Skoff, J. J. Hudson, B. E. Sauer, E. A. Hinds and M. R. Tarbutt, *Phys. Chem. Chem. Phys.*, 2011, **13**, 19013–19017.
31 D.-T. Nguyen, T. C. Steimle, I. Kozyryev, M. Huang and A. B. McCoy, *J. Mol. Spectrosc.*, 2018, **347**, 7–18.
32 A. C. Paul, K. Sharma, M. A. Reza, H. Telfah, T. A. Miller and J. Liu, *J. Chem. Phys.*, 2019, **151**, 134303.
33 T. A. Isaev and R. Berger, *Phys. Rev. Lett.*, 2016, **116**, 63006.
34 B. Rafei, G. Younes and M. Korek, *J. Phys.: Conf. Ser.*, 2017, **869**, 12001.
35 Q.-Q. Zhang, C.-L. Yang, M.-S. Wang, X.-G. Ma and W.-W. Liu, *J. Phys. B: At., Mol. Opt. Phys.*, 2018, **51**, 155102.

36 J. Cui, J.-G. Xu, J.-X. Qi, G. Dou and Y.-G. Zhang, *Chin. Phys. B*, 2018, **27**, 103101.
37 I. Zeid, T. Atallah, S. Kontar, W. Chmaisani, N. El-Kork and M. Korek, *Comput. Theor. Chem.*, 2018, **1126**, 16–32.
38 C. Li, Y. Li, Z. Ji, X. Qiu, Y. Lai, J. Wei, Y. Zhao, L. Deng, Y. Chen and J. Liu, *Phys. Rev. A*, 2018, **97**, 62501.
39 M. Li, J. Kłos, A. Petrov and S. Kotochigova, *Commun. Phys.*, 2019, **2**, 148.
40 Y. Hao, L. F. Pašteka, L. Visscher, P. Aggarwal, H. L. Bethlem, A. Boeschoten, A. Borschevsky, M. Denis, K. Esajas, S. Hoekstra, K. Jungmann, V. R. Marshall, T. B. Meijknecht, M. C. Mooij, R. G. E. Timmermans, A. Touwen, W. Ubachs, L. Willmann, Y. Yin and A. Zapara, *J. Chem. Phys.*, 2019, **151**, 34302.
41 M. V. Ivanov, F. H. Bangerter and A. I. Krylov, *Phys. Chem. Chem. Phys.*, 2019, **21**, 19447–19457.
42 H. Ladjimi, W. Zrafi, A.-R. Allouche and H. Berriche, *J. Quant. Spectrosc. Radiat. Transfer*, 2020, **252**, 107069.
43 M. V. Ivanov, F. H. Bangerter, P. Wójcik and A. I. Krylov, *J. Phys. Chem. Lett.*, 2020, **11**, 6670–6676.
44 M.-S. Xu, C.-L. Yang, M.-S. Wang, X.-G. Ma and W.-W. Liu, *J. Quant. Spectrosc. Radiat. Transfer*, 2020, **242**, 106770.
45 J. Kłos and S. Kotochigova, *Phys. Rev. Res.*, 2020, **2**, 13384.
46 A. L. Collopy, M. T. Hummon, M. Yeo, B. Yan and J. Ye, *New J. Phys.*, 2015, **17**, 55008.
47 M. Yeo, M. T. Hummon, A. L. Collopy, B. Yan, B. Hemmerling, E. Chae, J. M. Doyle and J. Ye, *Phys. Rev. Lett.*, 2015, **114**, 223003.
48 A. L. Collopy, S. Ding, Y. Wu, I. A. Finneran, L. Anderegg, B. L. Augenbraun, J. M. Doyle and J. Ye, *Phys. Rev. Lett.*, 2018, **121**, 213201.
49 S. Ding, Y. Wu, I. A. Finneran, J. J. Burau and J. Ye, *Phys. Rev. X*, 2020, **10**, 21049.
50 C. L. Chalek and J. L. Gole, *J. Chem. Phys.*, 1976, **65**, 2845–2859.
51 K. Liu and J. M. Parson, *J. Chem. Phys.*, 1977, **67**, 1814–1828.
52 C. Linton, *J. Mol. Spectrosc.*, 1978, **69**, 351–364.
53 A. Bernard and R. Gravina, *Astrophys. J., Suppl. Ser.*, 1983, **52**, 443–450.
54 T. C. Steimle and J. E. Shirley, *J. Chem. Phys.*, 1990, **92**, 3292–3296.
55 J. M. Badie and B. Granier, *Chem. Phys. Lett.*, 2002, **364**, 550–555.
56 J.-H. Leung, T. Ma and A. S. C. Cheung, *J. Mol. Spectrosc.*, 2005, **229**, 108–114.
57 D. Zhang, Q. Zhang, B. Zhu, J. Gu, B. Suo, Y. Chen and D. Zhao, *J. Chem. Phys.*, 2017, **146**, 114303.
58 N. R. Hutzler, H.-I. Lu and J. M. Doyle, *Chem. Rev.*, 2012, **112**, 4803–4827.
59 K. C. Cox, J. M. Weiner, G. P. Greve and J. K. Thompson, 2015 Joint Conference of the IEEE International Frequency Control Symposium the European Frequency and Time Forum, 2015, pp. 351–356.
60 S. L. Campbell, PhD thesis, University of Colorado Boulder, 2017.
61 J. F. Stanton, J. Gauss, L. Cheng, M. E. Harding, D. A. Matthews and P. G. Szalay, *CFOUR, Coupled-Cluster techniques for Computational Chemistry, a quantum-chemical program package*, with contributions from A. A. Auer, R. J. Bartlett, U. Benedikt, C. Berger, D. E. Bernholdt, Y. J. Bomble, O. Christiansen, F. Engel, R. Faber, M. Heckert, O. Heun, M. Hilgenberg, C. Huber, T.-C. Jagau, D. Jonsson, J. Jusélius, T. Kirsch, K. Klein, W. J. Lauderdale, F. Lipparini, T. Metzroth, L. A. Mück, D. P. O'Neill, D. R. Price, E. Prochnow, C. Puzzarini, K. Ruud, F. Schiffmann, W. Schwalbach, C. Simmons, S. Stopkowicz, A. Tajti, J. Vázquez, F. Wang, J. D. Watts and the integral packages MOLECULE (J. Almlöf and P. R. Taylor), PROPS (P. R. Taylor), ABACUS (T. Helgaker, H. J. A. Jensen, P. Jørgensen, and J. Olsen), and ECP routines by A. V. Mitin and C. van Wüllen. For the current version, see http://www.cfour.de.
62 D. A. Matthews, L. Cheng, M. E. Harding, F. Lipparini, S. Stopkowicz, T.-C. Jagau, P. G. Szalay, J. Gauss and J. F. Stanton, *J. Chem. Phys.*, 2020, **152**, 214108.
63 J. F. Stanton, J. Gauss, J. D. Watts and R. J. Bartlett, *J. Chem. Phys.*, 1991, **94**, 4334–4345.
64 J. D. Watts, J. Gauss and R. J. Bartlett, *J. Chem. Phys.*, 1992, **200**, 1–7.
65 L. Cheng and J. Gauss, *J. Chem. Phys.*, 2011, **135**, 084114.
66 D. A. Matthews, J. Gauss and J. F. Stanton, *J. Chem. Theory Comput.*, 2013, **9**, 2567–2572.
67 D. A. Matthews and J. F. Stanton, *J. Chem. Phys.*, 2015, **142**, 064108.
68 M. Nooijen and R. J. Bartlett, *J. Chem. Phys.*, 1995, **102**, 3629–3647.
69 J. H. Baraban, D. A. Matthews and J. F. Stanton, *J. Chem. Phys.*, 2016, **144**, 1–4.
70 J. F. Stanton and J. Gauss, *J. Chem. Phys.*, 1999, **111**, 8785–8788.
71 K. G. Dyall, *J. Chem. Phys.*, 2001, **115**, 9136–9143.
72 W. Liu and D. Peng, *J. Chem. Phys.*, 2009, **131**, 1–5.
73 C. Zhang and L. Cheng, *Mol. Phys.*, 2020, e1768313.
74 K. Klein and J. Gauss, *J. Chem. Phys.*, 2008, **129**, 194106.
75 E. Epifanovsky, K. Klein, S. Stopkowicz, J. Gauss and A. I. Krylov, *J. Chem. Phys.*, 2015, **143**, 064102.
76 L. Cheng, F. Wang, J. Stanton and J. Gauss, *J. Chem. Phys.*, 2018, **148**, 044108.
77 K. Raghavachari, G. W. Trucks, J. A. Pople and M. Head-Gordon, *Chem. Phys. Lett.*, 1989, **157**, 479–483.
78 R. J. Bartlett, J. D. Watts, S. A. Kucharski and J. Noga, *Chem. Phys. Lett.*, 1990, **165**, 513–522.
79 J. Liu, Y. Shen, A. Asthana and L. Cheng, *J. Chem. Phys.*, 2018, **148**, 034106.
80 K. G. Dyall, *J. Chem. Phys.*, 1997, **106**, 9618–9626.
81 M. Iliaš and T. Saue, *J. Chem. Phys.*, 2007, **126**, 64102.
82 J. Liu and L. Cheng, *J. Chem. Phys.*, 2018, **148**, 144108.
83 A. T. B. Gilbert, N. A. Besley and P. M. W. Gill, *J. Phys. Chem. A*, 2008, **112**, 13164–13171.
84 B. O. Roos, R. Lindh, P.-Å. Malmqvist, V. Veryazov and P.-O. Widmark, *J. Phys. Chem. A*, 2005, **109**, 6575–6579.

85 K. A. Peterson, D. Figgen, M. Dolg and H. Stoll, *J. Chem. Phys.*, 2007, **126**, 124101.
86 D. E. Woon and T. H. Dunning, Jr., *J. Chem. Phys.*, 1995, **103**, 4572–4585.
87 I. M. Mills, in *Molecular Spectroscopy: Modern Research*, ed. K. N. Rao and C. W. Mathews, Academic Press, New York, 1972, pp. 115–140.
88 D. T. Colbert and W. H. Miller, *J. Chem. Phys.*, 1992, **96**, 1982–1991.
89 S. R. Langhoff and C. W. Bauschlicher, *J. Chem. Phys.*, 1988, **89**, 2160–2169.
90 H. Lefebvre-Brion and R. W. Field, *The Spectra and Dynamics of Diatomic Molecules*, Elsevier, Amsterdam, 2004.
91 R. W. Field and T. H. Bergeman, *J. Chem. Phys.*, 1971, **54**, 2936–2948.
92 C. Li, L. Deng, Y. Zhang, L. Wu, X. Yang and Y. Chen, *J. Phys. Chem. A*, 2011, **115**, 2978–2984.
93 T. Helgaker, W. Klopper, H. Koch and J. Noga, *J. Chem. Phys.*, 1997, **106**, 9639–9646.
94 S. Ding, Y. Wu, I. A. Finneran, J. J. Burau and J. Ye, *Phys. Rev. X*, 2020, **10**, 021049.
95 M. A. Norcia, J. R. Cline, J. P. Bartolotta, M. J. Holland and J. K. Thompson, *New J. Phys.*, 2018, **20**, 023021.
96 J. P. Bartolotta, M. A. Norcia, J. R. Cline, J. K. Thompson and M. J. Holland, *Phys. Rev. A*, 2018, **98**, 023404.
97 S. Snigirev, A. J. Park, A. Heinz, I. Bloch and S. Blatt, *Phys. Rev. A*, 2019, **99**, 063421.
98 J. P. Bartolotta and M. J. Holland, *Phys. Rev. A*, 2020, **101**, 053434.
99 D. DeMille, *Phys. Rev. Lett.*, 2002, **88**, 067901.
100 K.-K. Ni, T. Rosenband and D. D. Grimes, *Chem. Sci.*, 2018, **9**, 6830–6838.
101 S. A. Moses, J. P. Covey, M. T. Miecnikowski, B. Yan, B. Gadway, J. Ye and D. S. Jin, *Science*, 2015, **350**, 659–662.
102 L. Anderegg, L. W. Cheuk, Y. Bao, S. Burchesky, W. Ketterle, K.-K. Ni and J. M. Doyle, *Science*, 2019, **365**, 1156–1158.
103 L. Caldwell and M. Tarbutt, *Phys. Rev. Res.*, 2020, **2**, 013251.
104 A. M. Kaufman, B. J. Lester and C. A. Regal, *Phys. Rev. X*, 2012, **2**, 041014.
105 M. Norcia, A. Young and A. Kaufman, *Phys. Rev. X*, 2018, **8**, 041054.
106 A. Cooper, J. P. Covey, I. S. Madjarov, S. G. Porsev, M. S. Safronova and M. Endres, *Phys. Rev. X*, 2018, **8**, 041055.
107 S. Saskin, J. Wilson, B. Grinkemeyer and J. Thompson, *Phys. Rev. Lett.*, 2019, **122**, 143002.
108 M. Heckert, M. Kállay and J. Gauss, *Mol. Phys.*, 2005, **103**, 2109–2115.
109 M. Heckert, M. Kállay, D. P. Tew, W. Klopper and J. Gauss, *J. Chem. Phys.*, 2006, **125**, 044108.